Molecular & Cellular Biomechanics
DOI: 10.32604/mcb.2019.07165
Article

Multifrequency Microwave Imaging for Brain Stroke Detection

Lulu Wang[1,*]

[1]Department of Biomedical Engineering, School of Instrument Science and Opto-electronics Engineering, Hefei University of Technology, Hefei, 230009, China

[*]Corresponding Author: Lulu Wang. Email: lwang381@hotmail.com; luluwang2015@hfut.edu.cn

Received: 04 May 2019; Accepted: 02 July 2019.

Abstract: CT and MRI are often used in the diagnosis and monitoring of stroke. However, they are expensive, time-consuming, produce ionizing radiation (CT), and not suitable for continuous monitoring stroke. Microwave imaging (MI) has been extensively investigated for identifying several types of human organs, including breast, brain, lung, liver, and gastric. The authors recently developed a holographic microwave imaging (HMI) algorithm for biological object detection. However, this method has difficulty in providing accurate information on embedded small inclusions. This paper describes the feasibility of the use of a multifrequency HMI algorithm for brain stroke detection. A numerical system, including HMI data collection model and a realistic head model, was developed to demonstrate the proposed method for imaging of brain tissues. Various experiments were carried out to evaluate the performance of the proposed method. Results of experiments carried out using multifrequency HMI have been compared with the results obtained from single frequency HMI. Results showed that multifrequency HMI could detect strokes and provide more accurate results of size and location than the single frequency HMI algorithm.

Keywords: Holographic microwave imaging; microwave imaging; brain stroke; dielectric object

1 Introduction

Early diagnosis of stroke with timely treatment could reduce adult permanent disability significantly [1]. Conventional medical imaging tools such as X-ray [2], positron emission tomography (PET) [3], ultrasound, computed tomography (CT), and magnetic resonance imaging (MRI) have been widely used for diagnosis of brain disease. Although CT is the current gold standard brain imaging tool, it has some limitations, including produce ionizing radiations, time-consuming, and not easy to identify early-stage abnormal tissue due to the relatively small dielectric proprieties contrast between the healthy tissue and abnormal tissue at X-ray frequencies [2]. More importantly, it is not suitable for continuously monitoring strokes and not easy to develop a portable system [5,6]. Therefore, developing a new screening method is urgently needed to improve the effectiveness of disease detection.

The use of microwave imaging (MI) for imaging of organs in particular breast and brain tissues has continuously attracted many researchers' interests over the past two decades [7,8]. The MI-based approaches are highly related to the dielectric properties difference between the normal and abnormal tissues at microwave frequencies. Microwaves do not use harmful ionizing radiation to generate images. Therefore MI-based approaches have the potential to become a safe biomedical imaging tool for detecting or monitoring the disease. Several MI algorithms and measurement systems have been developed for brain imaging [9-12]. Up to date, many MI methods based on Newton iterative [13], BIM [14], and Gauss-Newton approximations [15] have been developed to study brain tissue. A simplified head model includes stroke involved in these studies to numerically evaluate the potential of MI for brain imaging over the frequency range of 0.5 GHz ~ 2.5 GHz. The acute stroke with the size of 2cm could be successfully detected.

Recent clinical studies of MI suggested that more attention should be paid to develop a more sensitive imaging algorithm and clinical portable measurement device.

We previously developed a holographic microwave imaging (HMI) method for dielectric object detection with a particular focus on brain stroke [16]. Compared to the conventional microwave brain imaging method, HMI does not require massive computational works, which significantly reduce the computational cost. However, the existing HMI has difficulty in providing more accurate results on the diagnosis of inclusions, especially for small size. This paper investigates the feasibility of the use of multifrequency HMI for brain stroke detection. A numerical system was developed to demonstrate the proposed algorithm. Various experiments were carried out to evaluate the performance of the developed method, and the obtained results were compared with the obtained results of single frequency HMI.

2 Method

As shown in Fig. 1, the computer-guided multifrequency holographic microwave head imaging system consists of a microwave source generator, a transmitter, an N-element transceiver array, and a computer with an HMI image tool. All transceivers are positioned around the head phantom, and they are located on the same antenna array plane. During image data collection, the microwave signal generator continuously produces a microwave signal to the N-element transceiver array at a multifrequency range. The transceiver transmits microwave signals to the target head and records the backscattered electric fields from the head. The imaging progress includes transmit multifrequency microwave waves to the head and extract useful signals from the scattered signals, then use the proposed HMI algorithm to produce head images from backscattered signals.

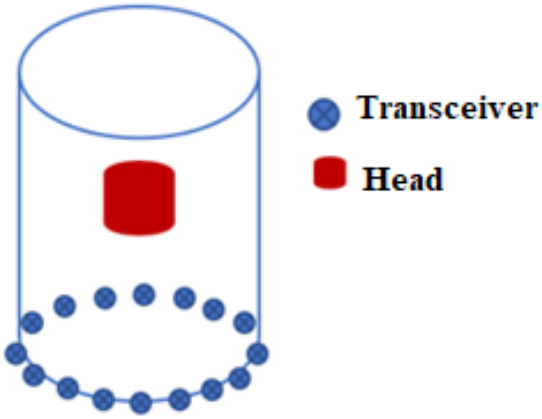

Figure 1: Multifrequency HMI setup

Let a target point TP locate in the head model (see Fig. 2), the scattering electric fields from the head namely visibility data can be measured by two transceivers located at A_i and A_j as [17]:

$$\vec{V}_{vi}^{(p,q)}(\vec{r_i},\vec{r_j}) =< \vec{E}_{scat}^{(p,q)}(\vec{r_i}) \cdot \vec{E}_{scat}^{*(p,q)}(\vec{r_j}) > \quad (1)$$

Where <> means the time average, $\vec{E}_{scat}^{(p,q)}$ is the scattering electric field, $\vec{E}_{scat}^{*(p,q)}$ denotes the conjugate complex of the scattering electric field, $p = 1, \dots, P$, $q = 1, \dots, Q$ at frequency $f^{(p)} = f_{min} + (p - \frac{1}{P} - 1)\Delta f$, f_{min}, Δf, P and Q are the minimum operation frequency, the operation frequency range, the number of frequencies, and the number of views, respectively.

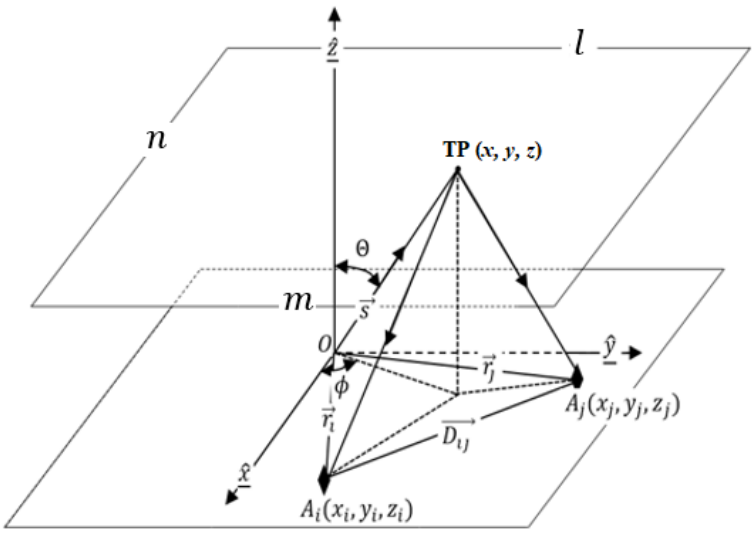

Figure 2: A pair of transceivers

Define the intensity of head as [16]:

$$\mathrm{I}^{(p,q)}(\vec{\mathrm{s}}) = \left(\frac{(2\pi f^{(p)}\sqrt{\varepsilon_b \mu_b})^2}{2}\right)^3 |\varepsilon_{\mathrm{r}}(\vec{\mathrm{s}}) - \varepsilon_b|^2 \vec{E}_T^{(p,q)}(\vec{\mathrm{s}}) \cdot \vec{E}_T^{*(p,q)}\left(\vec{s'}\right) \tag{2}$$

where ε_r denotes the relative permittivity of the head, ε_b is the relative permittivity of the host medium, ε_b and μ_b are the dielectric permittivity and magnetic permeability of the host medium, $\vec{\mathrm{s}}$ denotes the position vector, $\vec{E}_T^{(p,q)}$ is the total electric field and $\vec{E}_T^{(p,q)} = \vec{E}_{inc}^{(p,q)} + \vec{E}_{scat}^{(p,q)}$, $\vec{E}_{inc}^{(p,q)}$ being the incident electric field.

Eq. (3) is applied to simulate the visibility over the head:

$$\vec{V}_{vi}^{(p,q)}(\vec{r_i}, \vec{r_j}) = \left(\frac{(2\pi f^{(p)}\sqrt{\varepsilon_b \mu_b})^2}{2}\right)^3 \vec{E}_T^{(p,q)}(\vec{\mathrm{s}}) \cdot \vec{E}_T^{*(p,q)} \frac{e^{-j2\pi f^{(p)}\sqrt{\varepsilon_b \mu_b}(\vec{r_i} - \vec{r_j})\cdot \underline{\hat{s}}}}{s^2} \tag{3}$$

The above equation can be rewritten as:

$$\vec{V}_{vi}^{(p,q)}(\vec{D}_{ij}) = \iiint_v I^{(p,q)}(\vec{\mathrm{s}}) \frac{e^{-j2\pi \vec{D}_{ij}\hat{\mathrm{s}}}}{s^2} dV \tag{4}$$

where $\vec{D}_{ij} = (\vec{r}_j - \vec{r}_i)/\lambda_b$, λ_b is the host medium wavelength, $\underline{\hat{s}} = sin\theta cos\phi \underline{\hat{x}} + sin\theta sin\phi \underline{\hat{y}} + cos\theta \underline{\hat{z}}$.

In the spherical coordinate system, Eq. (4) becomes:

$$\vec{V}_{vi}^{(p,q)}(\vec{u}_{ij}, \vec{v}_{ij}, \vec{w}_{ij}) = \int_l \int_m \int_n \frac{I(s,l,m)}{\sqrt{1-l^2-m^2}} e^{-j2\pi \Phi_{ij}} dl dm ds \tag{5}$$

where $\Phi_{ij} = \vec{D}_{ij} \cdot s = \vec{u}_{ij} l + \vec{v}_{ij} m + \vec{w}_{ij} n$, $l = sin\theta cos\phi$, $m = sin\theta sin\phi$, and $n = cos\theta = \sqrt{1 - l^2 - m^2}$.

Eq. (6) is used to represent the visibility function as long as all transceivers located on the same flat plane.

$$\vec{V}_{vi}^{(p,q)}(\vec{u}_{ij}, \vec{v}_{ij}) = \iint I^{(p,q)}(l,m)\, e^{-j2\pi(\vec{u}_{ij} l + \vec{v}_{ij} m)} \tag{6}$$

An image can be reconstructed by:

$$I^{(p,q)}(l,m) = \iint \vec{V}_{vi}^{(p,q)}(\vec{u}_{ij}, \vec{v}_{ij})\, e^{j2\pi(\vec{u}_{ij} l + \vec{v}_{ij} m)} du dv \tag{7}$$

3 Numerical System

We developed a computer system, including the image data collection model and head model, to demonstrate the multifrequency HMI method. Several experiments were carried out using the numerical system to evaluate the accuracy of the proposed multifrequency HMI method for brain stroke detection. All simulations were performed using MATLAB 2018a on a Dell Precision 5820 workstation with Intel Xeon W-2145 CPU at 3.7 GHz and 256 GB of RAM.

A 16-element transceiver array was enclosed in the cubic shield, and all transceivers were regularly spaced and positioned around the head model. Each transceiver was simulated as transmitter and detector to transmit incident electric field to the head and to measure backscattered electric fields from the head. A matching medium ($\varepsilon_r = 58$, $\sigma_r = 0.48$ S/m) was filled in the space between the head and the transceiver array, and the frequency range of 1GHz~4GHz was selected as working frequencies [18-19]. The head and the transceiver array were positioned at z=0 mm and z=-50 mm and a 2D image dataset was recorded to produce a 2D image.

3.1 Forward Model Solution

In this study, a small waveguide antenna was simulated as the transceiver. The electric field radiated from such an antenna can be modeled as [20]:

$$\vec{E}_{inc}^{(p,q)}\left(\vec{\mathrm{R}}_{Tx},\theta,\phi\right) = \frac{-j2\pi f^{(p)}\sqrt{\varepsilon_b\mu_b}}{2\pi^2}\vec{E}_0^{(p,q)}\frac{e^{-j2\pi f^{(p)}\sqrt{\varepsilon_b\mu_b}\vec{\mathrm{R}}_{Tx}}}{\vec{\mathrm{R}}_{Tx}}ABh^{(p,q)}(\theta,\phi)\vec{P}^{(p,q)}(\theta,\phi) \tag{8}$$

where $\vec{\mathrm{R}}_{Tx}$ is the vector position from the head to the transmitter located at $\vec{\mathrm{R}}_{Tx}$, k_b denotes the wavelength number of the host medium, A and B are the board and narrow aperture of the waveguide, $h^{(p,q)}(\theta,\phi)$ is the radiation pattern, and $\vec{P}^{(p,q)}(\theta,\phi)$ denotes the polarization vector.

3.2 Backward Model Solution

The Born Approximation was applied to compute the backscattered fields. The backscattered fields measured by any receiver located at $\overrightarrow{r_m}$ [21]:

$$\vec{E}_{scat}^{(p,q)}(\overrightarrow{r_m}) = \frac{(2\pi f^{(p)}\sqrt{\varepsilon_b\mu_b})^2}{4\pi}\int_V |\varepsilon_r(\vec{\mathrm{s}}) - \varepsilon_b|^2[\vec{E}_{inc}^{(p,q)} - (\vec{E}_{inc}^{(p,q)}\cdot\overrightarrow{r_m})\overrightarrow{r_m}]\frac{\mathrm{e}^{-\mathrm{j}2\pi f^{(p)}\sqrt{\varepsilon_b\mu_b}\overrightarrow{r_m}}}{\overrightarrow{r_m}}dV \tag{9}$$

Where $\overrightarrow{r_m}$ is the vector position from the head to the receiver located at $\overrightarrow{r_m}$.

3.3 Head Model

Two sphere-shaped head phantoms ($200 \times 200 \times 100$ voxels) were developed using the Gaussian function to evaluate the proposed method. A sphere-shaped stroke was located in the head phantoms. Fig. 3 shows the real part (relative permittivity) and imaginary part (conductivities) of the head model I contains one stroke (a radius of 5 mm, squared in black) located at (0 mm, 0 mm, 0 mm). Fig. 4 shows the real part (relative permittivity) and imaginary part (conductivities) of head model II contains two strokes, where stroke A (a radius of 5 mm, squared in black) located at (0 mm, 0 mm, 0 mm) and stroke B (a radius of 3 mm, squared in black) located at (0 mm, 20 mm, 0 mm). Color bars in head model images (Fig. 3 and Fig. 4) demonstrate the permittivity and conductivity values of the head model.

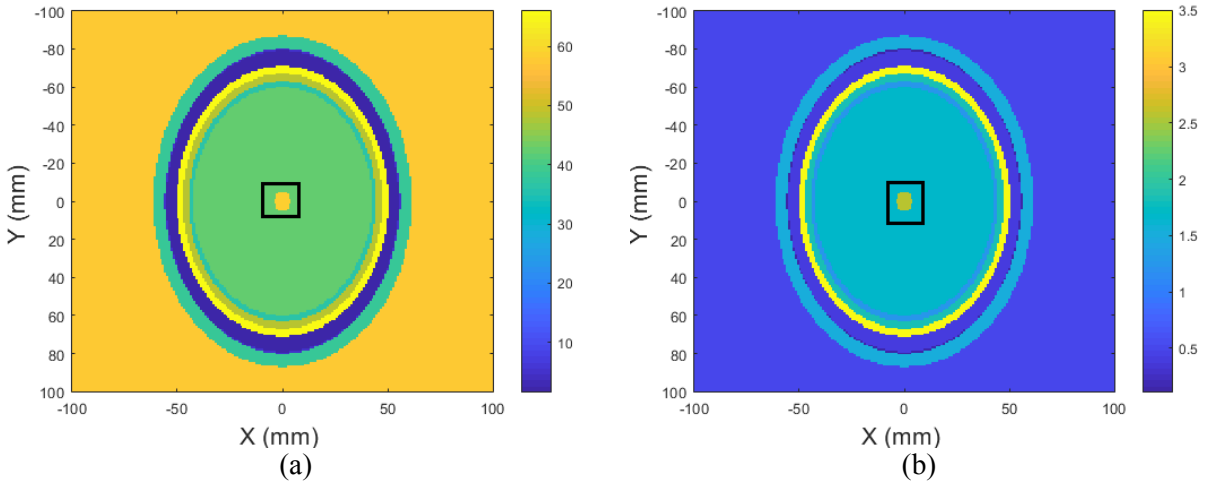

Figure 3: Head model I: (a) real part (relative permittivity); (b) imaginary part (conductivities)

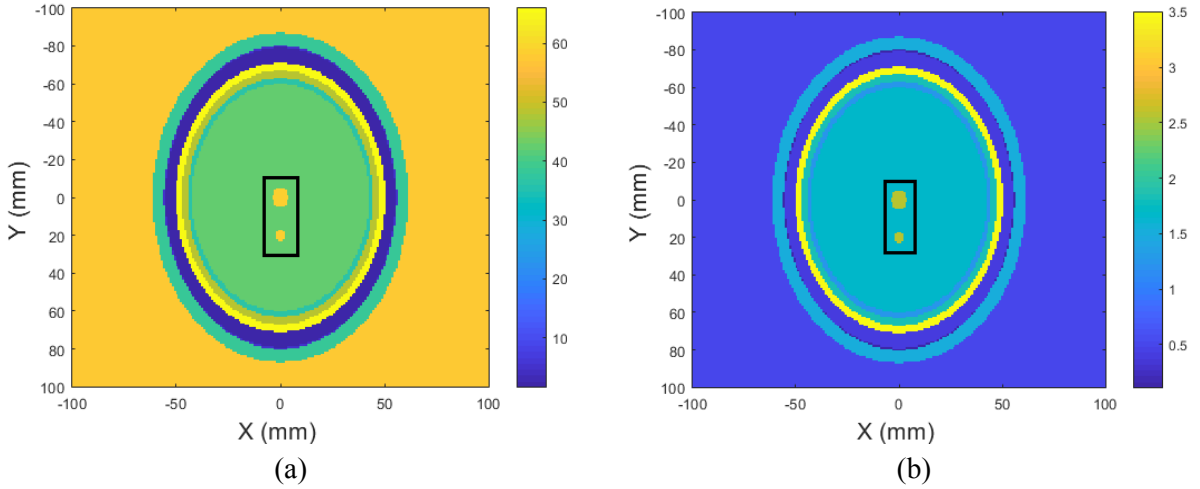

Figure 4: Head model II: (a) real part (relative permittivity); (b) imaginary part (conductivities)

4 Results and Discussion

Several simulation experiments were carried out by using MATLAB software to study the performance of the multifrequency HMI for brain stroke detection. According to the previous study [19], all simulation experiments were carried out over the frequency range of 1~4 GHz. The region under test is a cubic consist of head phantom and matching solution medium. In this study, 2D head images along the cross-range direction (XY plane) are presented to study the capabilities of the multifrequency HMI method.

Fig. 5 shows the reconstructed images of the head model I with the working frequency range of 1~4 GHz. The stroke could be clearly identified in the imaginary part of the reconstructed head image at the selected frequencies.

Fig. 6 illustrates the reconstructed images of head model II with the working frequency range of 1~4 GHz. Two strokes with different sizes and locations could be observed in the imaginary part of the reconstructed image. As shown in Fig. 5(a) and Fig. 6(a), strokes and internal structure of head models could not be detected in the real part of the reconstructed images. Therefore, we only present the imaginary part of the reconstructed head image in the following pages.

We also compared the multifrequency HMI with the single HMI algorithm. Figs. 7(a)-7(d) display the imaginary part of the reconstructed images of head phantom I with the frequency of 1 GHz, 2 GHz, 3 GHz, and 4 GHz, respectively. It can be seen that the stroke can be identified in the reconstructed head image

with the working frequency of 3 GHz. However, the single frequency HMI was failed to detect stroke with the working frequency of 1 GHz, 2 GHz, and 4 GHz. Color bars in reconstructed images (Figs. 5-7) present the backscattered energy density distributions of head models.

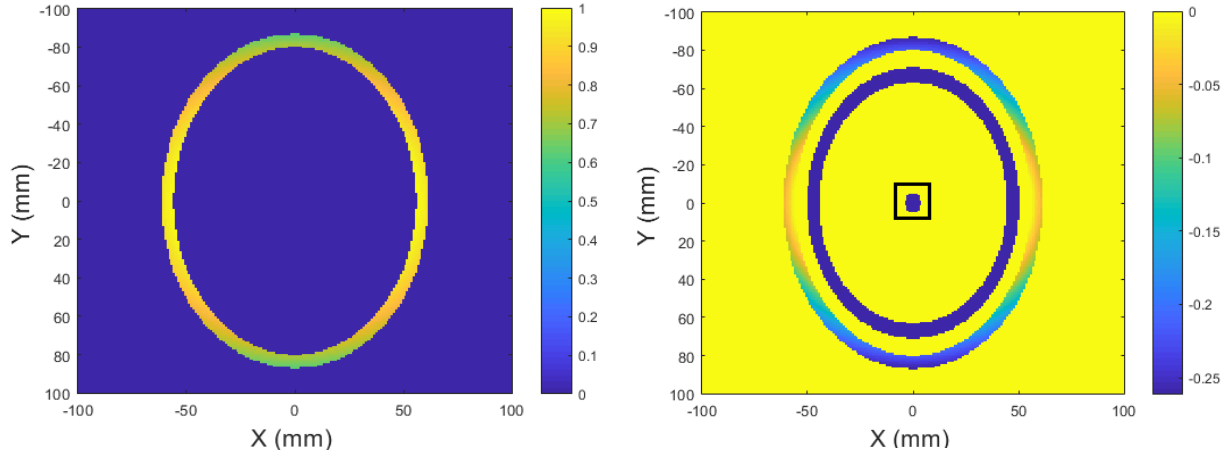

Figure 5: Reconstructed images of the head model I: (a) real part; (b) imaginary part

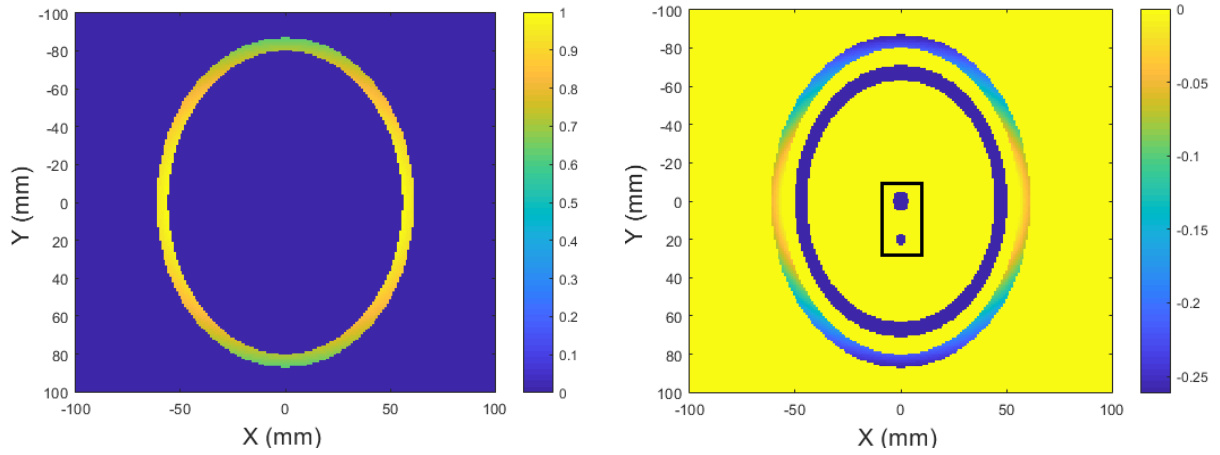

Figure 6: Reconstructed images of head model II: (a) real part; (b) imaginary part

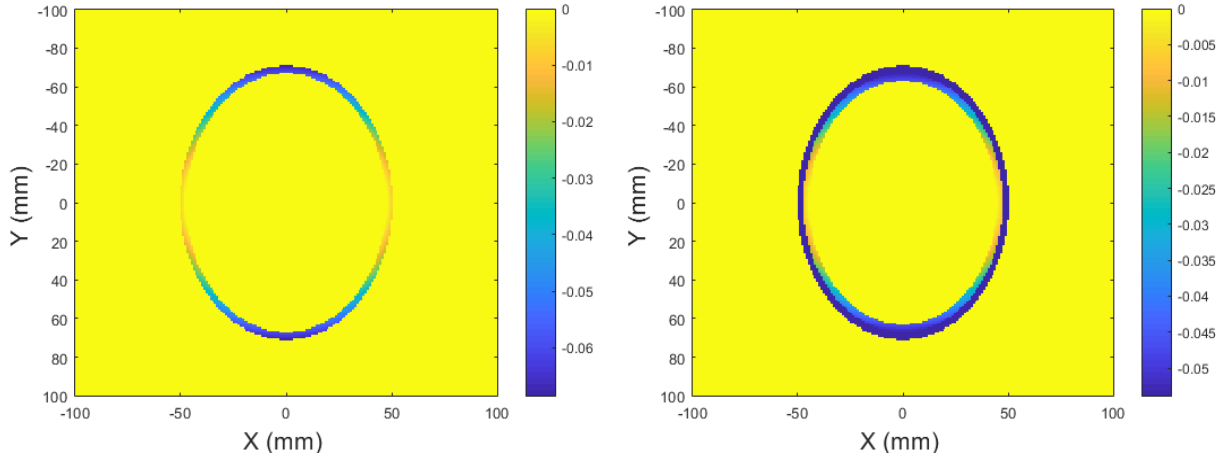

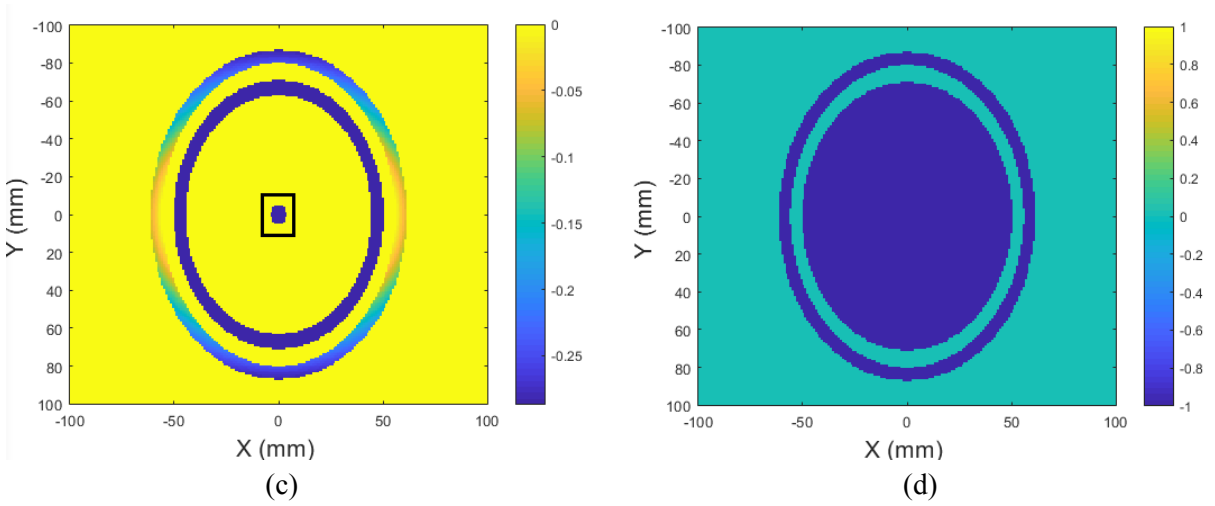

Figure 7: Reconstructed images of the head model I at: (a) 1 GHz; (b) 2 GHz; (c) 3 GHz; (d) 4 GHz

Unlike conventional medical imaging tools such as CT, microwave imaging is not considered to be suitable for full body imaging. Over the past few decades, investigators have focused their research on imaging of organs such as brain or breast that can be excited with low-power microwaves. An HMI system consists of an antenna array for performing measurements and a computer to display reconstructed images from the measured data. For a practical measurement system setup, a commercial vector network analyzer (VNA) can be used to continuously generate microwave source over the frequency range of 1-4 GHz with 250 MHz steps. Therefore, the HMI system can be driven by the commercial availability of high-performance VNA. The measured quantities are the scattering parameters (S-parameters). VNA produces a small power (limited to 10 mW) which is much lower than internationally recognized standards for mobile and wireless communication standards. Most of microwave imaging algorithms produce head images using 2D head models. The proposed method could produce head images from 3D head models, which offers much more accurate results than other microwave imaging methods. The development of multifrequency HMI measurement system and experimental validations on realistic head phantoms will be conducted in the future.

5 Conclusion

This paper investigated the feasibility of the use of multifrequency microwave imaging algorithm for brain stroke detection. A realistic computer system, including the data collection model and head model, was developed to evaluate the proposed method for brain stroke detection. The compassion study of multifrequency and single frequency microwave imaging methods was performed to validate the proposed method. The results demonstrated that the proposed algorithm could fully represent the internal head structures and more accurately detect strokes embedded in the multilayer head model. The proposed algorithm has the potential to become a useful image tool for accessing stroke.

Acknowledgement: This research was funded by the National Natural Science Foundation of China (Grant Nos. 61701159, JZ2017GJQN1131), the Natural Science Foundation of Anhui Province (Grant No. 101413246, JZ2017AKZR0129), the Fundamental Research Funds for the Central Universities (JZ2018HGTB0236), and the Ministry of Education of the People's Republic of China (Grant No. 2160311028).

Conflict of Interests: The authors declare that they have no conflicts of interest to report regarding the present study.

References

1. Ren CH, Gao MQ, Ning LI, Xun-Ming JI. Significance of biomarkers in stroke and research progress. *Military Medical Sciences* **2012**, 36(2): 150-153.
2. Mccann J, Stockton D, Godward S. Impact of false-positive mammography on subsequent screening attendance and risk of cancer. *Breast Cancer Research* **2002**, 4(5): R11.
3. Chibaudel B. Management of metastatic colorectal cancer. *Canadian Medical Association Journal* **2001**, 165(10): 1301-1301.
4. Frölich AM, Psychogios MN, Klotz E, Schramm R, Knauth M. et al. Angiographic reconstructions from whole-brain perfusion CT for the detection of large vessel occlusion in acute stroke. *Stroke* **2012**, 43(1): 97-102.
5. Brazzelli M, Sandercock PAG, Celani MG, Righetti E, Chappell FM et al. MRI versus CT for detection of acute vascular lesions in patients presenting with stroke symptoms. *Stroke* **2010**, 41(5): E427-E428.
6. Almirall H, Broquetas A, Jofre L. Active microwave computed brain tomography: the response to a challenge. *Journal of Neuroscience Methods* **1991**, 36(2-3): 239.
7. Wang L. Electromagnetic induction holography imaging for stroke detection. *Journal of the Optical Society of America A Optics Image Science & Vision* **2017**, 34(2): 294.
8. Semenov SY, Corfield DR. Microwave tomography for brain imaging: feasibility assessment for stroke detection. *International Journal of Antennas & Propagation* **2008**, 4: 264-276.
9. Tournier PH, Bonazzoli M, Dolean V, Rapetti F, Hecht F. et al. Numerical modeling and high-speed parallel computing: new perspectives on tomographic microwave imaging for brain stroke detection and monitoring. *IEEE Antennas & Propagation Magazine* **2017**, (99): 1.
10. Tournier PH, Hecht F, Nataf F, Bonazzoli M, Rapetti F et al. Microwave tomography for brain stroke imaging. *IEEE International Symposium on Antennas and Propagation & Usnc/ursi National Radio Science Meetin*g **2017**, 29-30.
11. Mahmood Q, Li S, Fhager A, Candefjord S, Chodorowski A et al. A comparative study of automated segmentation methods for use in a microwave tomography system for imaging intracerebral hemorrhage in stroke patients. *Journal of Electromagnetic Analysis & Applications* **2015**, 7(5): 152-167.
12. Scapaticci R, Bucci OM, Catapano I, Crocco L. Differential microwave imaging for brain stroke followup. *International Journal of Antennas & Propagation* **2014**, 6: 1-11.
13. Bisio I, Fedeli A, Lavagetto F, Pastorino M, Randazzo A. et al. Microwave data inversion in hemorrhagic brain stroke imaging: a newton-conjugate-gradient based approach in Lp Banach spaces. *IEEE Conference on Antenna Measurements & Applications* **2017**, 275-278.
14. Ireland D, Bialkowski K, Abbosh A. Microwave imaging for brain stroke detection using born iterative method. *IET Microwaves Antennas & Propagation* **2013**, 7(11): 909-915.
15. Mojabi P, Lovetri J. Microwave biomedical imaging using the multiplicative regularized gauss-newton inversion. *IEEE Antennas & Wireless Propagation Letters* **2009**, 8(4): 645-648.
16. Wang L, Al-Jumaily AM, Simpkin R. Holographic microwave imaging array for brain stroke detection. *Journal of Signal and Information Processing* **2013**, 4(3B): 96-101.
17. Levanda R, Leshem A. Synthetic aperture radio telescopes. *IEEE Signal Processing Magazine* **2010**, (27)1: 14-29.
18. Italian National Research Council. An internet resource for the calculation of the dielectric properties of body tissues in the frequency range 10 Hz-100 GHz. Accessed on May. 4, 2019.
19. Scapaticci R, Bucci OM, Catapano I, Crocco L. Differential microwave imaging for brain stroke followup. *International Journal of Antennas and Propagation* **2014**, 1-11.
20. Wang L, Al-Jumaily AM, Simpkin R. Imaging of 3-D dielectric objects using far-field holographic microwave imaging technique. *Progress in Electromagnetics Research B* **2014**, 61: 135-147.
21. Silver, S. Microwave Antenna Theory and Design. *S. Peter Peregrinus Ltd.*, London, UK, **1984**.